LIMNOLOGY
and
OCEANOGRAPHY: METHODS

Limnol. Oceanogr.: Methods 8, 2010, 507–526

Using laser diffraction data to obtain accurate particle size distributions: the role of particle composition

Stephen Andrews, Daniel Nover, and S. Geoffrey Schladow*
Department of Civil and Environmental Engineering, University of California, Davis, CA 95616, USA

Abstract

Suspended particle composition has a large influence on light scattering by small (<20 μm) particles. Inorganic particles and organic phytoplankton cells, both common in natural waters, have very different indices of refraction. This can affect results from laser diffraction particle size analyzers, which measure light scattering and assume an index of refraction to calculate the particle size distribution. Here we examine the effect of the assumed index of refraction on laser diffraction data. A Laser In-situ Scattering and Transmissometry (LISST) 100X instrument is used to record scattered light distributions from glass microspheres, phytoplankton monocultures, and natural particle samples of mixed composition. The scattering distributions are processed with kernel matrices, derived using Mie theory, assuming either organic or inorganic compositions. Resulting particle size distributions are compared against microscope images. Processing with an assumed inorganic index of refraction was found to produce the most accurate results over the majority of the samples tested. The effect of scattering by particles having diameters outside the instrument inversion range was also assessed. The presence of significant concentrations of particles exceeding the upper limit of the LISST range (>250 μm) produced little effect; however, particles smaller than the lower limit (<1.25 μm) influenced concentrations over the entire LISST size range and produced counterintuitive effects, such as increased concentrations in the largest size bins.

Accurate measurement of the particle size distribution (PSD) in natural waters is central to a wide range of disciplines in science and engineering. Research includes understanding or predicting estuarine sediment transport (Gartner et al. 2001), phytoplankton community dynamics (Karp-Boss et al. 2007), large scale fluid motions (Rienecker et al. 2008), contaminant fate and transport (Hipsey et al. 2006), flocculation and aggregation patterns (Fettweis 2008), and the optical properties of water (Agrawal 2005). The characteristics of the particles of concern in these areas span the range of particle variability in natural waters. Particle composition can vary from mineral grains to live phytoplankton cells to heterogeneous flocs. Particle size may vary from colloidal suspensions with median diameters below 1 μm to flocs several millimeters in length, and particle shape can vary from spherical to highly complex (Stramski et al. 2004).

Laser diffraction instruments are a popular means of measuring PSDs because of their ease of use, non-PSD-specific calibration, and speed, in comparison to other techniques such as sieving, image processing, or the use of acoustic sensors (Pedocchi and Garcia 2006a). They have been shown to produce accurate results for a wide range of particle sizes, shapes, and compositions (Jones 1999). The development of the Laser In-Situ Scattering and Transmissometry (LISST) series instruments has advanced the laser diffraction technique by providing reliable, real-time, in-situ measurements of PSDs in natural waters (Agrawal and Pottsmith 2000). This has allowed uncertainties due to aggregation, floc breakup, or organic growth during the transport and handling of samples to be removed from size distribution calculations, and has also allowed for long-term, continuous monitoring applications.

Laser diffraction instruments project a laser beam through a sample containing particles in suspension, measure the light scattered at a range of small forward angles, and back-calculate the PSD using an assumed optical model. The optical model

*Corresponding author: E-mail: swandrews@ucdavis.edu

Acknowledgments

This research was supported by the UC Davis Tahoe Environmental Research Center. The authors would like to thank Y. Agrawal and H.C. Pottsmith at Sequoia Scientific for their clarifications of LISST operating principles and procedures, and M. Winder and B. Allen at TERC for their help in obtaining phytoplankton cultures and environmental samples. We also thank D. Hunter for microscope help, and E. Litchman, S. Nichol, K. Ger, and J. Waller for maintaining the cultures used in this study. Comments and suggestions from E. Boss and an anonymous reviewer helped improve the manuscript significantly.

DOI 10.4319/lom.2010.8.507

may be based on analytic theory or empirical data and is used to predict the distribution of light scattered by particles of a specific size onto the range of angles measured by the instrument's photodetectors. In practice, the optical model takes the form of a kernel matrix, K_{ij}. Each column, j, of the matrix contains the scattering signature—the distribution of light scattered across the angles, i, measured by the photodetectors—for a particular size class. The concentration of particles in each size class, V_j, is computed from the total scattered energy sensed by each photodetector, E_i, by solving the matrix equation $E_i = K_{ij}V_j$.

For many laser diffraction instruments, Mie theory is used as the optical model. Mie theory is robust, placing no restrictions on particle size, and is easily calculable with current computer resources. Suspended particles are assumed spherical, and Maxwell's equations for propagation of electromagnetic radiation are solved analytically to predict the intensity of light scattered by a particle. Results depend on the incident light wavelength, scattering angle under consideration, and particle diameter and refractive index (Bohren and Huffman 1983). The refractive index, m, is intrinsic to the particle's material composition and has both real and imaginary parts, $m = n + ki$. The real part, n, is used to quantify changes in light propagation that occur when light passes between the particle and its surrounding medium. The imaginary part, k, quantifies absorption of light by the particle. For particles suspended in water, the refractive index is generally defined relative to water and that convention is used here. Phytoplankton cells, because they comprise mostly water, have low refractive indices. Values for the real part of the complex refractive index range from 1.02–1.07, and vary with the species under consideration (Aas 1996). Common mineral particles such as quartz, feldspars, and clays have higher real refractive indices—in the range of 1.14–1.20 (Klein 2002). Absorption between the two particle types differs as well. Phytoplankton cells have a generally higher imaginary component of the refractive index, because they contain light-absorbing chlorophyll pigments.

A common misconception is that the effects of the refractive index on light scattering are small at the range of forward angles measured by laser diffraction instruments, making the sizing technique invariant to particle composition. This assumption is justified for particle sizes above approximately 20 µm but is incorrect for finer particles. In Fig. 1, light scattering, as predicted by Mie theory, is shown for 2, 10, and 30 µm diameter particles of two compositions—one with a refractive index approximating that of an algal cell (m = 1.05 + 0.004i) and the other approximating an inorganic mineral grain (m = 1.17 + 0.0001i). The magnitude and width of the principle scattering lobe are the features which have the largest impact on PSD calculations. The large differences seen in these features for 2 µm particles will thus produce a significant impact on laser diffraction results.

Sequoia Scientific, manufacturer of the LISST series instruments, provides users with a kernel matrix computed using

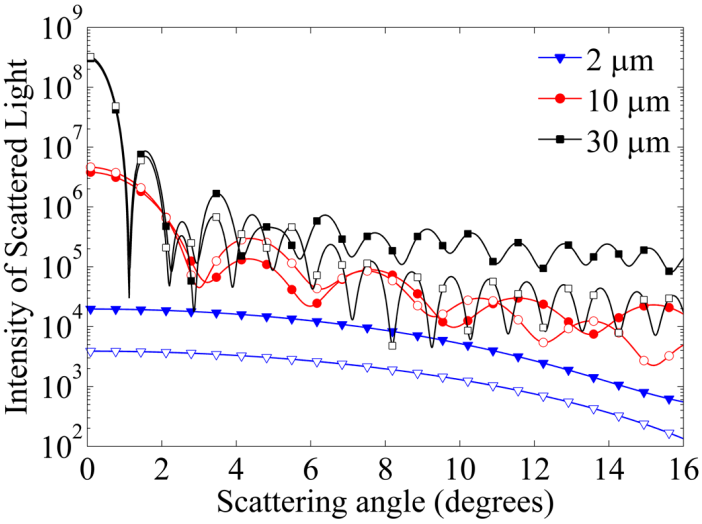

Fig. 1. Mie theory predicted light scattering as a function of sphere size and composition. Open symbols denote particles with a refractive index representative of a phytoplankton cell (m = 1.05 + 0.004i), and filled symbols indicate particles with a refractive index representative of a mineral grain (m = 1.17 + 0.0001i). Data are shown for a light wavelength of 670 nm, and scattered light intensity is given in relative units.

Mie theory for use in their data processing software. For the smallest size classes, kernel matrix scattering signatures are calculated as a combination of several different indices of refraction, to make the processed results generalizable for a wide range of particle compositions (Agrawal pers. comm. 2009). Recently, Sequoia Scientific has also created and distributed a second kernel matrix, based on empirical observations of light scattering by random shaped particles. As described in Agrawal et al. (2008), river sediment samples were collected, separated into isolated fractions corresponding to the LISST size classes, and the light scattering signature for each class was determined using the LISST. Individual class signatures were then combined to create the random shape kernel matrix. This work implied that for environments where the bulk of particles are randomly shaped inorganic grains (for example, a river or nearshore coastal environment), processing with the random shaped matrix will produce more accurate results.

In this study, we continue with the line of reasoning set forth by Agrawal et al. (2008) and test whether a priori knowledge of the bulk particle composition can be used to calculate more accurate PSDs through the use of kernel matrices tailored to a specific index of refraction. We collect raw scattering distributions using a LISST 100X instrument for glass bead samples, pure phytoplankton cultures, and field samples, concentrating mainly on particles on the fine end of the LISST measurement range (1.25–20 µm). The scattering distributions are processed using the kernel matrices provided by the manufacturer as well as matrices created using Mie theory with specific indices of refraction. Results are evaluated against PSDs obtained through microscopy.

The theory and data processing routines developed for this study also afforded the opportunity to examine the theoretical response of the LISST to particles outside its inversion range (1.25–250 µm). Although the LISST range encompasses a large proportion of the sizes relevant to aquatic studies, natural particle populations contain significant concentrations below 1.25 µm and above 250 µm. Two broad classes of organic particulates, picophytoplankton and heterotrophic bacteria, are common constituents of natural waters and are often smaller than 1.25 µm. Large flocs encountered in coastal waters routinely exceed 250 µm, the upper limit of the LISST Type B instrument, and often 500 µm, the upper limit of the Type C instrument. While it has been assumed that out-of-range particles affect the nearest measurable size bins, little work has been done to explicitly characterize these effects. Small out-of-range particles are briefly noted to have influenced LISST fine particle measurements by Traykovski et al. (1999), but no quantification of their effects was given. Mikkelsen (2002) addressed the effect of large out-of-range particles on the LISST through the use of a Malvern MasterSizer/E but did not perform any tests on the LISST itself. We conclude this study with a theoretical estimate of LISST errors associated with out-of-range particles. Mie theory is used to build scattering signatures for particles outside the inversion range, and PSD results for the field samples are recalculated assuming varying out-of-range particulate concentrations.

Materials and methods

LISST instrument fundamentals—A LISST 100X Type B instrument is used for all experiments reported here. The operating details and technical specifications are described in Agrawal and Pottsmith (2000), but are briefly reviewed here for clarity. The LISST provides particle volume concentrations, in units of µL/L, for 32 size bins between 1.25 and 250 µm. The range of diameters covered by each size bin increases geometrically by a factor of $200^{1/32} \approx 1.18$ with increasing diameter, so that the first bin spans the range 1.25 to 1.47 µm whereas the last bin includes particles from 212 to 250 µm. The LISST measures light scattering by directing a 670 nm, collimated laser beam through a sample volume of length 5 cm. A small portion of laser is directed into a photodetector before reaching the sample volume to measure laser output power, which may fluctuate in response to changes in instrument temperature. Light scattered by particles in suspension is measured by 32 concentric photosensitive ring detectors on the opposite side of the sample volume. The ring detectors span the scattering angle range of 0.07° to 14.2° in water, and the widths of the ring detectors increase geometrically, with each adjacent outer ring being 1.18 times the width of the inner ring. A separate detector at the center of the rings measures the transmitted laser power. This, divided by the output laser power, gives the bulk transmission of the sample, T, and is used to calculate the sample attenuation coefficient, c, using $T = \exp(-c\,L)$, where L is the path length.

Before scattered light distributions are inverted to obtain the PSD, they must first be corrected to account for background, non-particulate scattering due to pure water and instrument optics (Agrawal and Pottsmith 2000). Let z_i be the scattered power sensed by the i^{th} photodetector in a pure water sample, let T_{pw} be the transmission, and let P_{pw} be the output laser power. The raw scattering measured during an experiment, $\hat{E}_i$, must first be de-attenuated

$$\tilde{E}_i = \frac{\hat{E}_i}{\left(T / T_{pw}\right)} \tag{1}$$

and corrected for fluctuations in output laser power

$$\bar{E}_i = \frac{\tilde{E}_i}{\left(P_{pw} / P\right)} - z_i \tag{2}$$

before the background scatter is removed (Slade and Boss 2006). The final corrected scattering, E_i, is obtained by multiplying by factors, g_i, which account for the non-ideal responsivity of each ring detector to light, $E_i = g_i\,\bar{E}_i$. These factors are instrument specific and provided by the manufacturer.

The size distribution, V_j, is obtained from the matrix equation

$$E_i = C_v K_{ij} V_j \tag{3}$$

where C_v is an instrument specific conversion factor, accounting for integration constants, instrument electronics, and instrument optics (Agrawal and Pottsmith 2000). A matrix inversion must be performed to solve equation 3.

$$V_j = \frac{1}{C_v}\left(K_{ij}^{-1} E_i\right) \tag{4}$$

The inversion problem is difficult because the kernel matrix is intrinsically ill-conditioned (Hirleman 1987). As a result, inversion algorithms for laser diffraction devices are the subject of ongoing research, and equation 4 may be solved using, for example, the modified Chahine method (Riley and Agrawal 1991) or the projection methods of Pedocchi and Garcia (2006b) or Shen et al. (2008). Given the same inputs, each method will produce slightly different results and display different sensitivities to data noise, but testing by the authors showed the modified Chahine method to produce the fastest, most stable results. All inversions performed in this work were thus made with the modified Chahine method, using MATLAB (release 2009a) routines provided by Sequoia Scientific.

Kernel matrix calculations—The kernel matrix K_{ij} contains the information needed to convert the scattered power sensed by ring detectors into suspended particle concentrations. The j^{th} column contains the specific light scattering signature that

a particle from the j^{th} size class is expected to produce, based on an assumed optical model. The superposition of the product of all 32 of these scattering signatures and their bin concentrations produces the original scattering distribution detected by the LISST.

Scattering of a specific light wavelength by a natural particle is known to depend on the particle's size, shape, orientation, and composition (Bohren and Huffman 1983). Mie theory assumes that particles are spherical and of homogeneous composition, but places no restrictions on particle size or material. Maxwell's equations describing the electromagnetic fields within and surrounding the particle are solved analytically, and the intensity of scattered light in two perpendicular directions of vibration, S_1 and S_2, is predicted as a function of the scattering angle, particle diameter, and refractive index. In the case of unpolarized source light, the total scattered light intensity is proportional to $S_{11} = 1/2\ (|S_1|^2 + |S_2|^2)$. The entries in the kernel matrix can be calculated by

$$K_{ij} = \frac{1}{d_{j,\max} - d_{j,\min}} \int_{d_{j,\min}}^{d_{j,\max}} \int_{\theta_{i,\min}}^{\theta_{i,\max}} \frac{1}{d_j^3} S_{11}(d_j, m, \theta) \sin\theta \, d\theta \, dd \quad (5)$$

where d_j is a diameter within the j^{th} size class, θ_i is an angle covered by the i^{th} photodetector, and m is the complex refractive index (Traykovski et al. 1999). In equation 5, the scattering intensity is integrated over the range of angles subtended by the i^{th} ring detector and averaged over the range of diameters within the j^{th} size class. The factor d_j^3 is used to relate scattering predicted for individual particles to the LISST output of particle volume concentrations. Analytical formulas for the light intensities, S_1 and S_2, along with a well-established Fortran program used to calculate them, are given in Bohren and Huffman (1983).

It should be mentioned that the LISST laser output is linearly polarized, contrary to what was assumed above, and the rings photodetectors are nonpolarized. As pointed out by Slade and Boss (2006), this means that the intensity of scattered light sensed by the detectors will be additionally influenced by the S_{12} and S_{13} terms in the Mueller scattering matrix. Because the LISST photodetectors do not cover the full range of azimuthal angles (they cover only 60°), equation 5 without azimuthal integration and the inclusion of S_{12} and S_{13} is not strictly correct. Slade and Boss (2006) quantified this departure from the nonpolarized light assumption for spherical scatterers using the magnitude of the polarization factor, $|S_{12}/S_{11}|$. Values for this factor were generally found to be less than 0.1, although they peaked at the largest angle rings. Azimuthal integration and the additional matrix elements can easily be incorporated into equation 5 if the relative angle between the polarization plane and the photodetector azimuthal range is known. Unfortunately, the LISST uses a fiber-coupled laser and the polarization direction may rotate at random in response to small changes in temperature or mechanical stress (Pottsmith pers. comm. 2010). Becuase these dependencies are not known, we have neglected their effects and assumed azimuthal symmetry. An estimate of error from this assumption is given in the microsphere results section.

The light intensities S_1 and S_2 may alternatively be calculated for a *nonspherical* particle using *T*-matrix theory, a generalization of Mie theory to nonspherical particles of homogeneous composition (Waterman 1965; Mishchenko et al. 1996). A *T*-matrix Fortran program, detailed in Mishchenko and Travis (1998), is freely available online to calculate scattering from cylinders or ellipsoids, averaged over a set of random particle orientations, with results reported using the equivalent spherical diameter (ESD) of the particle. While the theory applies to particles of arbitrary aspect ratios, computations for large particles with extreme aspect ratios are hampered by non-convergence. Methods of approximating the *T*-matrix results for particles of intermediate and large sizes are available (e.g., the geometrical optics approximation), but were not used in this study, because most particles considered fell within the *T*-matrix computational limits.

In optical studies, it is convenient to separate the full range of aquatic particles into two groups, organic and inorganic, based on their optical properties (Clavano et al. 2007). The organic particle group includes living material, such as bacteria, phytoplankton, and zooplankton, and non-living material, such as dead algal cells and organic detritus. Particles in this group are composed mostly of water, but also contain light-absorbing pigments. As a result, they have low refractive indices but are considered strong absorbers, with absorption indices in the range of 0.002–0.007 near 670 nm (Stramski et al. 2001). The inorganic particle group includes lithogenic and biogenic minerals and has relatively high refractive indices and low absorptions. Here we consider two particle compositions: (1) a typical organic particle, with composition represented using a complex refractive index of $m = 1.05 + 0.004i$, and (2) a typical inorganic particle, with a refractive index of $m = 1.17 + 0.0001i$. The values of these indices are taken as representative of the two particle groups, following the work of Clavano et al. (2007).

Five kernel matrices were used in the data conversions—two provided by the LISST manufacturer, two calculated using Mie theory, and one calculated using *T*-matrix theory. The matrices are described as follows:

1. Sequoia Scientific provided spherical matrix, calculated with Mie theory as a composite of several refractive indices and designed for general application to a wide range of natural particles. This matrix will be referred to as the Mie composite matrix.
2. Sequoia Scientific provided random shape matrix, with individual class scattering signatures derived empirically from random shaped inorganic mineral grains. This matrix will be referred to as the random shape matrix.
3. Mie theory calculated matrix, with a complex index of refraction $m = 1.05 + 0.004i$, representative of a phytoplankton cell. This matrix will be referred to using the real part of the refractive index as the $n = 1.05$ matrix, for brevity.

4. Mie theory calculated matrix, with a complex index of refraction $m = 1.17 + 0.0001i$, representative of an inorganic sediment particle. This matrix will be referred to as the $n = 1.17$ matrix.
5. *T*-matrix theory calculated matrix, for small ellipsoids with a length-to-diameter ratio of 2.0 and an index of refraction equal to the $n = 1.05$ matrix, designed to simulate scattering from ellipsoidal phytoplankton cells.

All calculated matrices were derived using 50 intermediate diameters per size bin and a constant angle spacing of 0.0018° in equation 5. This resulted in seven intermediate angles within the smallest LISST ring, and approximately 1200 intermediate angles within the largest. Predicted light intensities were calculated using the Mie theory [vectorized "fastmie" implementation by Slade and Boss (2006)] and *T*-matrix theory programs mentioned previously.

Kernel matrices 1 through 4 are shown graphically in Fig. 2. Each curve shows the scattered light distribution for a particular size class over all 32 LISST ring detectors. The largest size classes show principle scattering peaks at the smallest ring

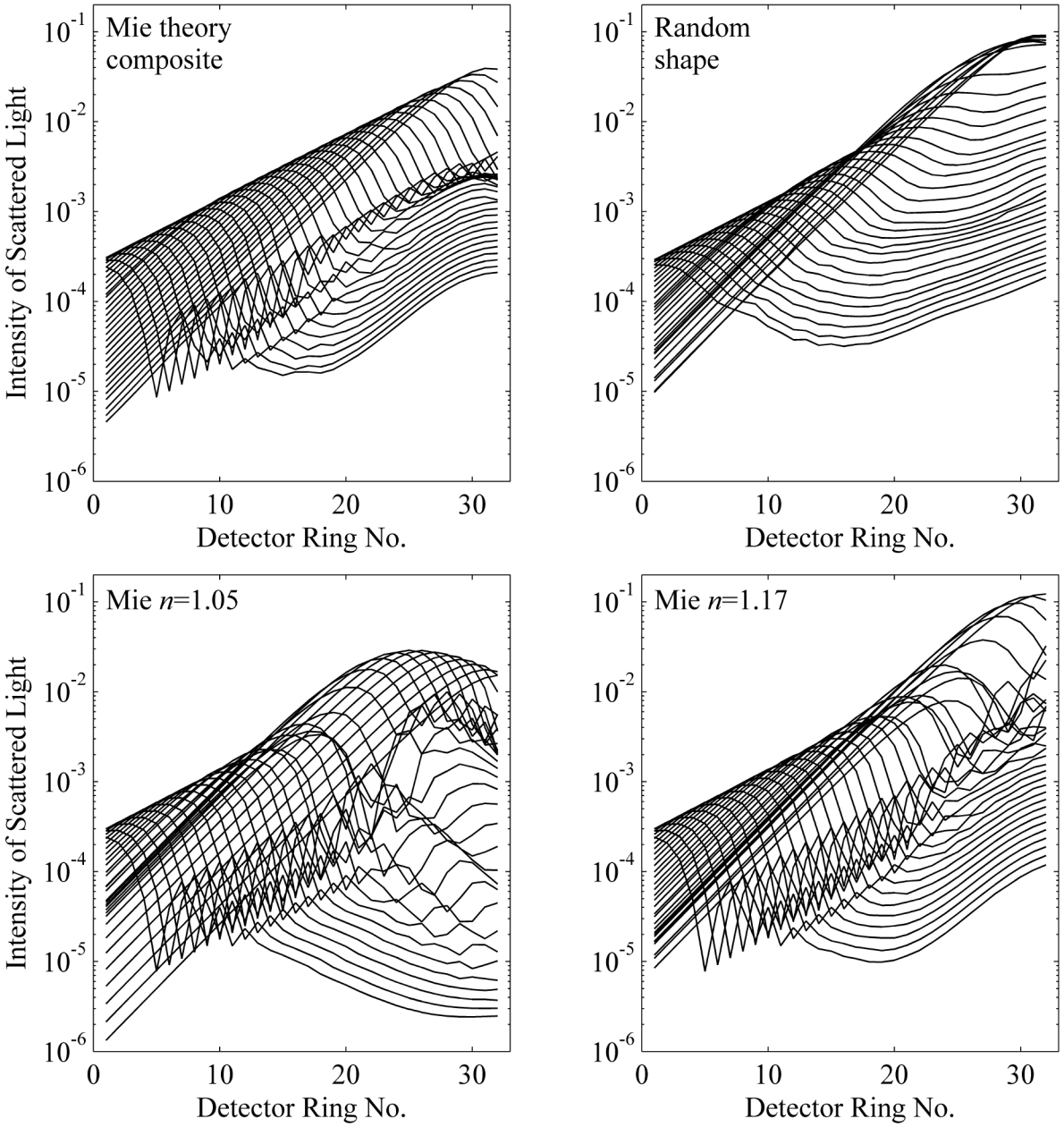

Fig. 2. Graphical illustration of kernel matrices used in this study. Curves correspond to scattering signatures for each of the 32 particle size classes measured by the LISST. Curves for the small size classes show intensity peaks in the high ring detectors, whereas large size classes display peaks in the small ring detectors. Light intensity is given in relative units.

numbers, corresponding to the smallest scattering angles. Scattering signatures are roughly consistent in the peak magnitudes of their principle scattering lobes across Mie theory calculated matrices for approximately the largest 17 size bins. This roughly corresponds to particles above 20 µm. Below 20 µm, particle index of refraction influences peak values appreciably. For the *T*-matrix theory derived matrix (not shown) calculations for ESD size classes above 13 µm were numerically unstable. Scattering signatures for ellipsoids with a length to diameter ratio of 1.33 were used for classes between 13 µm and 21 µm, and spherical calculations were made for particles above 21 µm. The matrix was similar in shape to Matrix 3, but with broader principle peaks and less pronounced secondary peaks in the smallest particle classes.

Assessment

Glass bead samples—Kernel matrix processing effects were first tested using six inorganic microsphere distributions. Three samples were comprised of monodisperse, borosilicate glass spheres of mean diameters 2.0, 5.6, and 8.0 µm, traceable by the National Institute of Standards and Technology (NIST), and listed as having an index of refraction of $n = 1.17$. A fourth sample was composed of monodisperse polystyrene [$n = 1.19$, from Ma et al. (2003)] flow cytometry reference beads of mean diameter 2.5 µm. The final two samples were polydisperse, one consisting of hollow glass beads with diameters between 2 and 20 µm, and the other consisting of 25–32 µm solid glass beads. The latter were provided by Sequoia Scientific with the purchase of our LISST 100X for instrument validation purposes. Bead sample characteristics are summarized in Table 1.

All bead samples were diluted to between 70% and 90% transmission, as measured by the LISST, using Milli-Q ultrapure water and were run on the LISST in bench-top mode. Samples were energetically mixed before pouring into the LISST sample chamber, and recirculation pumping was not needed, as settling effects were small for the particle size range tested. Measurements were recorded as the average of 10 laser bursts at 1 s intervals for approximately 100 s, and raw scattering distributions were corrected using an ultrapure water blank, taken before sampling using the procedure described previously. Each corrected scattering distribution was then converted to four distinct PSDs using Matrices 1 through 4. The PSDs were filtered to remove any measurements where one or more size class recorded a significantly negative concentration (< –0.01 µL/L) and were averaged over time to obtain final PSDs.

A concentrated subsample of each bead distribution, obtained before dilution, was analyzed using a Zeiss Axio Observer A1 light microscope. Concentrated subsamples were necessary to decrease the number of digital images needed to analyze a sufficient number of beads. Between 10 and 30 digital images were taken for each distribution at magnifications between 100× and 400×. The images were analyzed using routines in the Matlab Image Processing Toolbox to determine bead diameters. At least 1000 beads were analyzed for each sample (Table 1), and the resulting size distribution was binned to correspond with the LISST size classes. Particle number concentrations were then converted to volume fractions by multiplying by the volume of the geometric mean diameter of each size bin.

The resulting PSDs, which were derived from higher concentration samples than were run on the LISST, were scaled to the LISST samples using the following procedure. For each sample, the image analysis PSD was converted to an attenuation coefficient using the relation

$$c_{\text{im}} = \sum_{j=1}^{32} N_j Q_{\text{ext},j} A_j \tag{6}$$

where N_j is number of particles in the j^{th} size class, A_j is the particle cross-sectional area, and $Q_{\text{ext},j}$ is the extinction efficiency (Bohren and Huffman 1983). The extinction efficiency is the ratio of incident light area scattered or absorbed by a particle to its cross-sectional area. For scattering by glass beads, it can be calculated using Mie theory with the program given in Bohren and Huffman (1983) and oscillates around an average value of 2. Extinction values used in equation 6 were calculated as the average of the efficiencies for 20 intermediate diameters within each class. For the 2–20 µm hollow microspheres, the coated sphere code given in Bohren and Huffman (1983) was used (Matlab implementation by Adleman [2009]). Image derived volume concentrations in each size bin were then multiplied by the scalar factor $c_{\text{lisst}}/c_{\text{im}}$, where c_{lisst} is the attenuation measured for the LISST sample to obtain the final PSD predicted by image analysis.

An easier way of scaling the microscope PSD to the LISST-

Table 1. Bead sample characteristics. Image analysis parameters are given in the far right columns.

Nominal diameter	Company	Stock number	Mean diameter or range	Material	Magnification	Approximate no. of beads analyzed
2 µm	Duke Scientific	9002	2.0 ± 0.5 µm	Glass	400X	11040
2.5 µm	Invitrogen	P-14825	2.5 ± 0.25 µm	Polystyrene	400X	1680
5 µm	Duke Scientific	9005	5.6 ± 0.5 µm	Glass	400X	1740
8 µm	Duke Scientific	9008	8.0 ± 0.8 µm	Glass	200X	1560
2–20 µm	Polysciences	19823	2–20 µm	Hollow glass	100X	4680
25–32 µm	Sequoia Scientific	—	25–32 µm	Glass	100X	1430

measured concentrations would be to use the dilution rate. However, previous research (Pedocchi and Garcia 2006a) and our own experience demonstrate that insufficient mixing of samples within the cuvette is often a problem. The recorded attenuation values, which correlate very well with total particulate cross-sectional area, are a more accurate estimation of the concentration the LISST is actually measuring in the sample chamber. For this reason, attenuation based scaling is used for all the samples presented here. For monodisperse NIST traceable samples, the total bead concentration from scaled image analysis PSDs matched the expected concentrations based on the dilution rate to within 30%. We note that the use of attenuation ratio based scaling may bias the results of polydisperse samples. In these cases, the coarser size fraction will settle out faster than the fine fraction, resulting in LISST PSDs skewed toward fine particles. Scaling of the unaffected microscope PSD to a LISST attenuation coefficient measured after some of the coarse fraction has settled out may create a microscope PSD that is scaled artificially low. However, for the sample time scales (≈100 s) and size fractions (generally < 20 μm), this effect is expected to be small, and examinations of the transmission time series showed relatively constant values over the duration of each sample.

Results from the microsphere bead standards are shown in Fig. 3. Two things are apparent from the 2.5, 5, 8, 2–20, and 25–32 μm results. First, the random shape matrix produces a mean diameter 1–2 bins too large; this effect was observed in both the monodisperse and polydisperse samples. Second, processing with the n = 1.05 and Mie composite matrices produces large numbers of particles in the smallest bins, which were not observed under the microscope. Twenty-five percent of the total volume concentration in the 5 μm, n = 1.05 PSD was erroneously created in the two smallest size classes. Twenty-three percent was created for the 8 μm sample. For results processed with the Mie theory composite matrix, 6% and 7% of the volume was erroneously created. Peak diameters were generally consistent through the Mie theory derived matrices, although the n = 1.17 matrix more accurately predicted the mean diameter of the 2.5 μm beads.

We calculated total volume concentrations for each bead sample for both the microscope image PSD and each of the four LISST results. This was done to assess the bulk performance of each kernel matrix. Ratios of total LISST volume concentration to total microscope volume concentration, averaged over the six bead samples, were 1.47, 0.96, 1.90, and 1.08 for the Mie composite, random shape, n = 1.05, and n = 1.17 matrices, respectively. In the 2 μm bead sample, all methods underpredicted the mean diameter, placing it in the smallest bin. The peak concentrations for the n = 1.17 and random shape PSDs were much closer, however, than the n = 1.05 and composite PSDs to microscope results.

The monodisperse microsphere results from the n = 1.17 matrix were chosen to assess the sensitivity of calculated concentrations to variation in the index of refraction. Results are shown in Fig. 4. Variation associated with the assumption of unpolarized source light was also examined by deriving a kernel matrix, which accounted for the S_{12} Mueller matrix element (the S_{13} element approaches zero for spherical particles), resulting from polarized light, and integration over azimuth angles from 0°–60°

$$K_{ij} = \frac{1}{d_{j,\max} - d_{j,\min}} \int_{d_{j,\min}}^{d_{j,\max}} \int_{\theta_{i,\min}}^{\theta_{i,\max}} \int_{\phi=0}^{\phi=\frac{\pi}{3}} \frac{1}{d_j^3} (S_{11} + \cos(2\phi) S_{12}) \sin\theta \, d\phi \, d\theta \, dd \tag{7}$$

where S_{12} = 1/2 ($|S_2|^2$ - $|S_1|^2$) and ϕ is the azimuth angle. Recalculated PSDs were largely insensitive to variation in the imaginary part of the refractive index and the assumption of polarized source light. An order of magnitude increase in the imaginary part of the refractive index altered total concentrations by less than 2%. Enforcing the polarized light constraint affected concentrations by less than 1%. Variation in the real part of the refractive index produced a significant effect though, and perturbations of ±0.02 changed total concentrations by up to 20% but were generally less than 5%; the largest sensitivity was seen in the 2.5 μm beads, and decreased with increasing bead diameter. None of the minor refractive index variations tested significantly affected the shape of the PSD.

Phytoplankton cultures—LISST measurements were conducted on 6 phytoplankton monocultures. The samples represent 3 major classes of algae (cyanobacteria, chlorophytes, and diatoms) and were cultured from standard strains obtained from the University of Texas Culture Collection of Algae (UTEX), the University of Toronto Culture Collection of Algae and Cyanobacteria (UTCC), and the Chlamydomonas Center (CC). All samples represent genera commonly found in aquatic ecosystems. Four of the species exist in culture as isolated cells and have cell shapes that are either roughly spherical (*Pseudomonas fluorescens*, *Microcystis aeruginosa*, and *Chlamydomonas reinhardtii*) or ellipsoidal (*Synechococcus elongatus*). The two diatom species (*Asterionella formosa* and *Fragilaria crotonensis*) have highly nonspherical individual cells that join together to form complex colonies. The cells of *A. formosa* are roughly cylindrical, with a length-to-diameter ratio of approximately 3, and form two-dimensional colonies where individual cells connect in the center and radiate out, similar to the shape of an asterisk (*). *F. crotonensis* cells are shaped like elongated square prisms, with a length-to-width ratio of about five, and connect side to side to form long, ribbon-like chains. Phytoplankton strain and morphology information is summarized in Table 2.

Phytoplankton samples were run on the LISST in a manner similar to the beads, although samples were mixed less energetically to prevent cell damage. Each corrected scattering distribution was processed using Matrices 1 through 4 to generate four PSDs. The *S. elongatus* sample was additionally processed using Matrix 5, derived for scattering by ellipsoids.

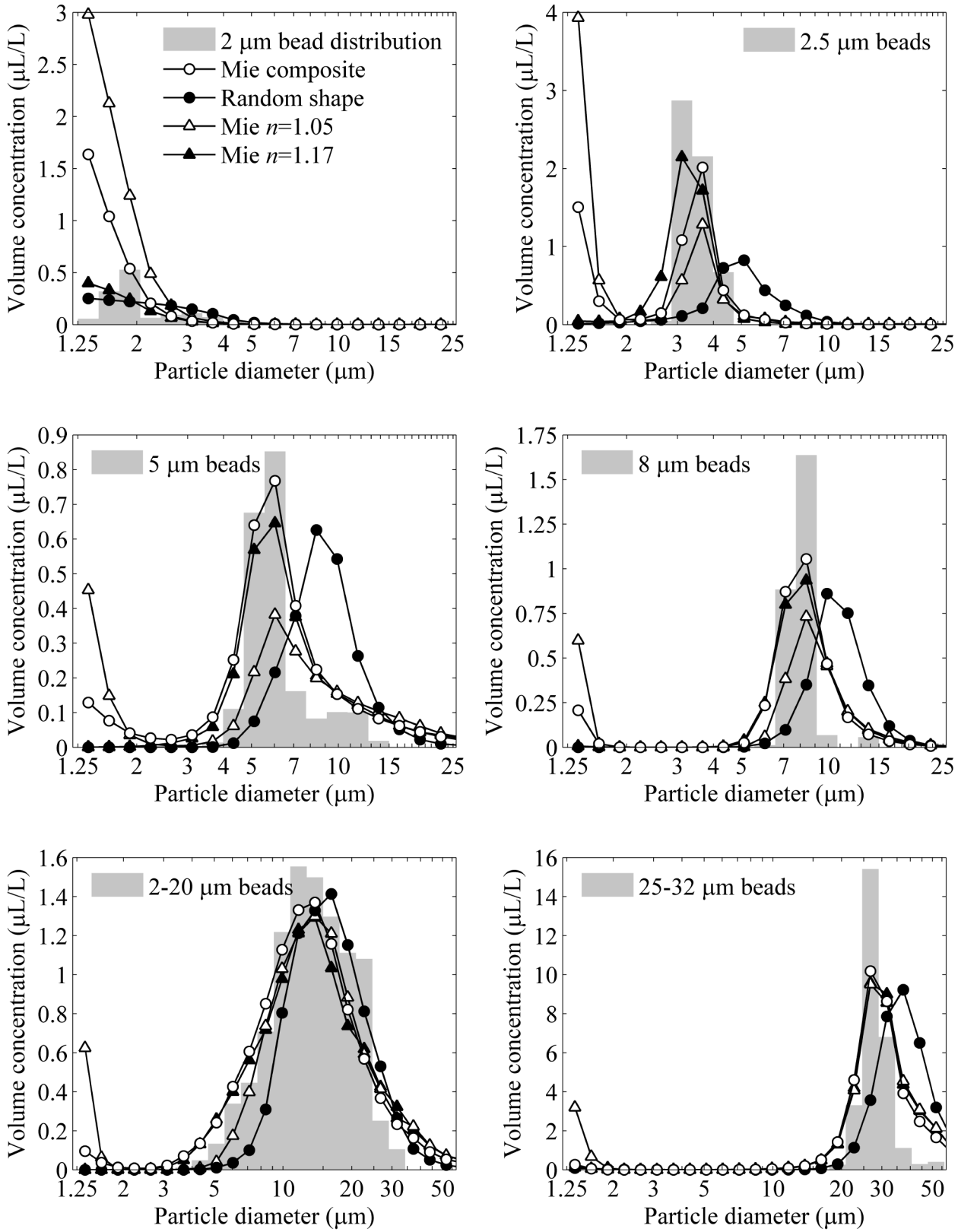

Fig. 3. Microsphere bead PSDs obtained from microscopy (shaded bars) and laser diffraction data processed using different kernel matrices. Three matrices are derived from Mie theory with refractive indices, n = 1.05, n = 1.17, and the average of a range of values (Mie composite). The final matrix is derived from empirical observations on randomly shaped particles.

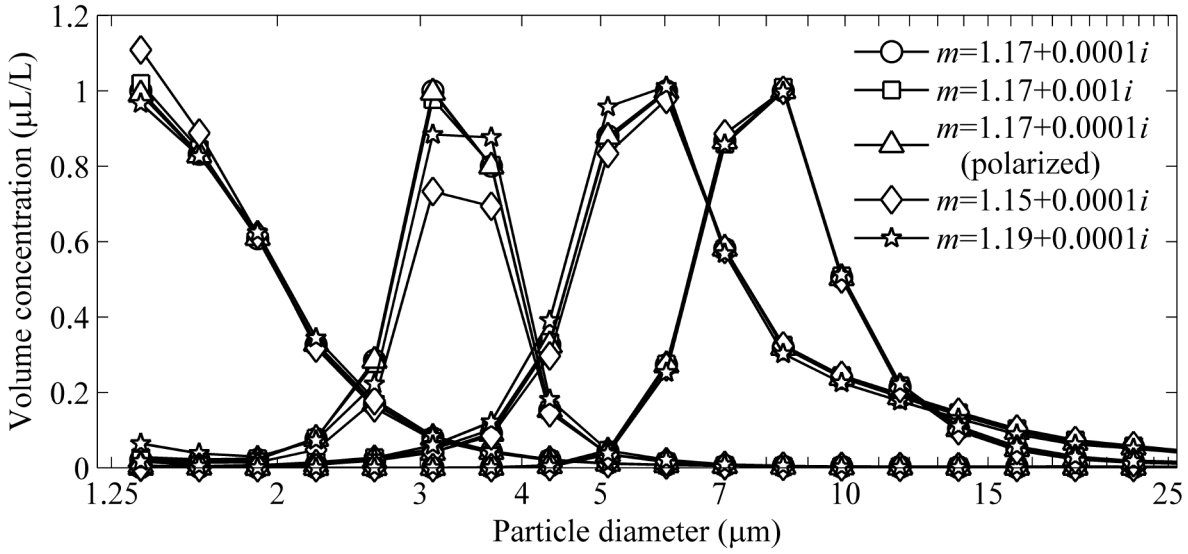

Fig. 4. Sensitivity of monodisperse microsphere bead PSDs to small changes in the real and imaginary parts of the index of refraction. The matrix labeled $m = 1.17 + 0.0001i$ (polarized) was derived assuming polarized source light and a fixed polarization plane to ring detector offset of 0°.

Table 2. Phytoplankton sample strain and morphology information.

Species	Class	Strain	Cell shape	Mean ESD	Colony-forming
Pseudomonas fluorescens	Cyanobacteria	CL145A	Sphere	1.0 μm	–
Microcystis aeruginosa	Cyanobacteria	UTEX 2386	Sphere	2.5 μm	–
Chlamydomonas reinhardtii	Chlorophyta	CC 2935	Sphere	6.5 μm	–
Synechococcus elongatus	Cyanobacteria	UTEX 625	Ellipsoid	3.0 μm	–
Asterionella formosa	Diatom	UTCC 605	Pennate	–	+
Fragilaria crotonensis	Diatom	UTEX 496	Pennate	–	+

For the spherical species, microscope images were taken as described for the beads, and image processed PSDs were scaled to LISST attenuation values using equation 6. The Mie theory derived extinction efficiencies, $Q_{ext,i}$, needed for this were recalculated using $m = 1.05 + 0.004i$. Although the cells were not perfectly spherical, Mie theory closely approximates non-spherical particles with aspect ratios near one (Clavano et al. 2007). For the ellipsoidal *S. elongatus* sample, cell lengths, *L*, and diameters, *d*, were measured from microscope images of approximately 200 cells. For each cell, the length and diameter were used to calculate an ellipsoid volume,

$$V_{el} = \frac{4\pi}{3}\left(\frac{d}{2}\right)^2 \frac{L}{2}, \tag{8}$$

which was then used to calculate an equivalent spherical diameter,

$$d_{esd} = 2\sqrt{\frac{3}{4\pi} V_{el} \frac{2}{L}}. \tag{9}$$

The size distribution of the ESDs was computed, scaled using extinction efficiencies calculated from *T*-matrix theory, and compared with the LISST derived PSDs. For the colony-forming diatom species, measurements were taken from microscope images of between 50 and 100 cells to determine the size distribution of cell lengths and colony diameters (*A. formosa*) or chain width and thickness (*F. crotonensis*). No ESD calculations were attempted for these two species.

Results processed using Mie theory on the spherical algae species *M. aeruginosa* and *C. reinhardtii* show good agreement with microscope results on the mean diameter location (Fig. 5). This is consistent with data presented in Karp-Boss et al. (2007), who found a similar agreement between the LISST and microscopy on other spherical algal species. The random shape matrix overpredicted the cell diameter, similar to the bead samples. Also similar to the bead samples, the $n = 1.05$ and composite matrix results showed fine particles in the smallest size bins that were not seen in the microscope images. All matrices underpredicted microscope-measured total volume concentration for *M. aeruginosa* but were more accurate for *C. reinhardtii*. LISST to microscope total volume concentration ratios were 1.07, 0.71, 0.72, and 0.77 for the Mie composite, random shape, $n = 1.05$, and $n = 1.17$ matrices, respectively, averaged over the two samples.

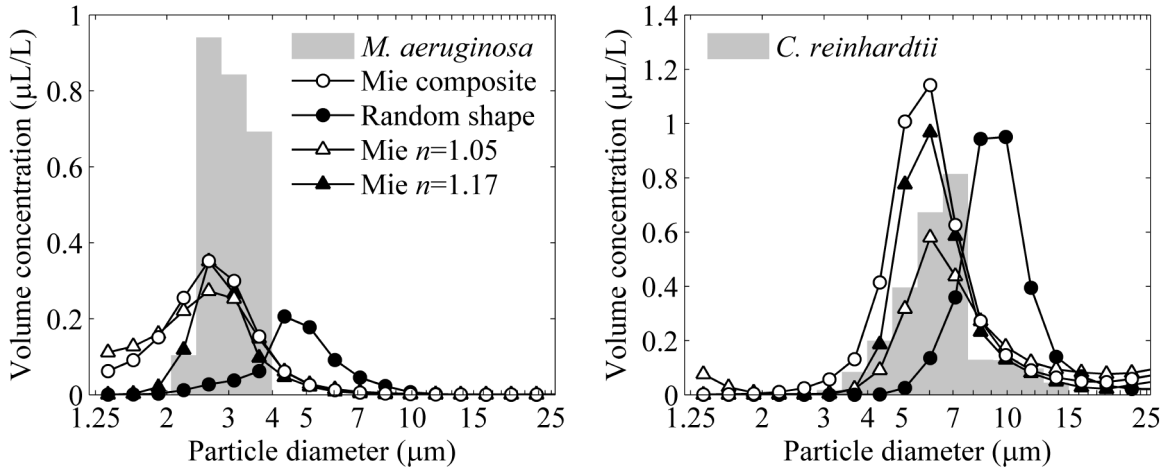

Fig. 5. Spherical algae species PSDs obtained through microscopy (shaded bars) and laser diffraction data processed using 4 kernel matrices, as in Fig. 3.

The microscope and processed LISST results for the phytoplankton species *P. fluorescens* are shown in Fig. 6. *P. fluorescens* belongs to the picophytoplankton algal group, classified by average cell diameters between 0.2 and 2 µm. Microscope results on *P. fluorescens* indicated an average cell diameter ≈0.8 µm, well below the lower LISST detection limit. Cell diameters below 1.25 µm were binned into an additional 5 geometrically spaced size classes to facilitate comparisons with the LISST data. The n = 1.17 and random shape matrices produced volume concentrations in the first size bins similar to the microscope derived results, whereas the n = 1.05 and composite matrix results were much higher.

Results for *S. elongatus*, the first significantly nonspherical sample studied, are presented in Fig. 7. Microscope results show the peak ESD located at 2.7 µm, with average cell dimensions of 2.0 µm (diameter) and 4.5 µm (length). All processing matrices underestimated the cell dimensions, instead locating the concentration peak in the smallest bin. The *T*-matrix kernel, for which the scattering signature of each size class below 13 µm was calculated assuming an equivalent volume ellipsoid of aspect ratio 2.0, showed similar results to the matrix derived from spherical particles of the same refractive index. Ratios of total LISST measured volume concentration to microscope derived volume concentration were 0.81, 0.34, 1.42, and 0.36 for the Mie composite, random shape, n = 1.05, and n = 1.17 matrices, respectively. Concentrations were significantly underestimated by the random shape and n = 1.17 matrices and overestimated by the n = 1.05 matrix. We also calculated the total cross-sectional area concentration, in units of m^{-1}, for the microscope and LISST results. Laser diffraction instruments measuring forward scatter are known to be more sensitive to particle cross-sectional area than particle volume (Bohren and Huffman 1983; Karp-Boss et al. 2007). Ratios of LISST to microscope total cross-sectional area were 3.46, 0.98, 6.50, 1.23, respectively, for the kernel matrices in the order listed before.

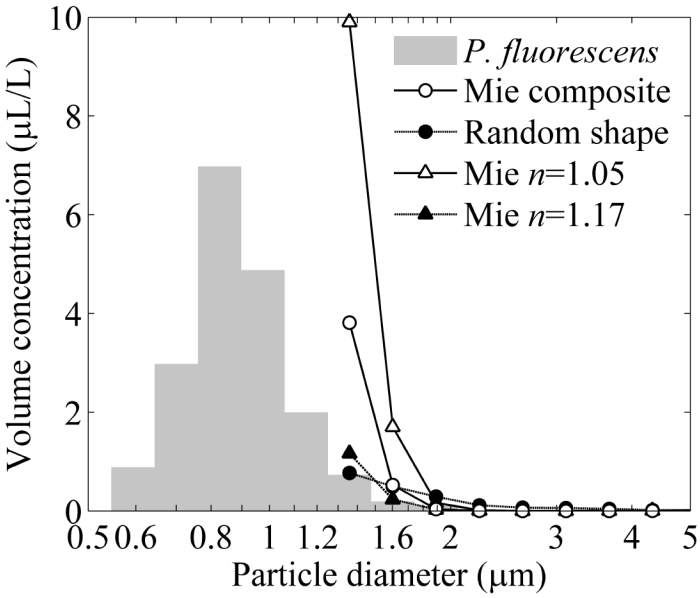

Fig. 6. Picophytoplankton *P. fluorescens* PSDs obtained through microscopy (shaded bars) and laser diffraction data processed using 4 kernel matrices, as in Fig. 3.

LISST processed PSDs for the chain-forming diatom cultures show broad peaks at diameters well above cell/colony ESDs or prominent cell/colony dimensions (Fig. 8). Local maxima were seen at smaller sizes and corresponded to the cell length and colony diameter in *A. formosa*. The prominence of the cell length peak in the *A. formosa* PSDs was likely due to the presence of incomplete colonies of 3-5 cells connected side to side. These were seen frequently in the microscope images. The PSD results for *F. crotonensis* showed one local maximum that did not correspond to any prominent cell dimension and another corresponding to the average cell length. The average cell width, which was approximately the same as the thickness

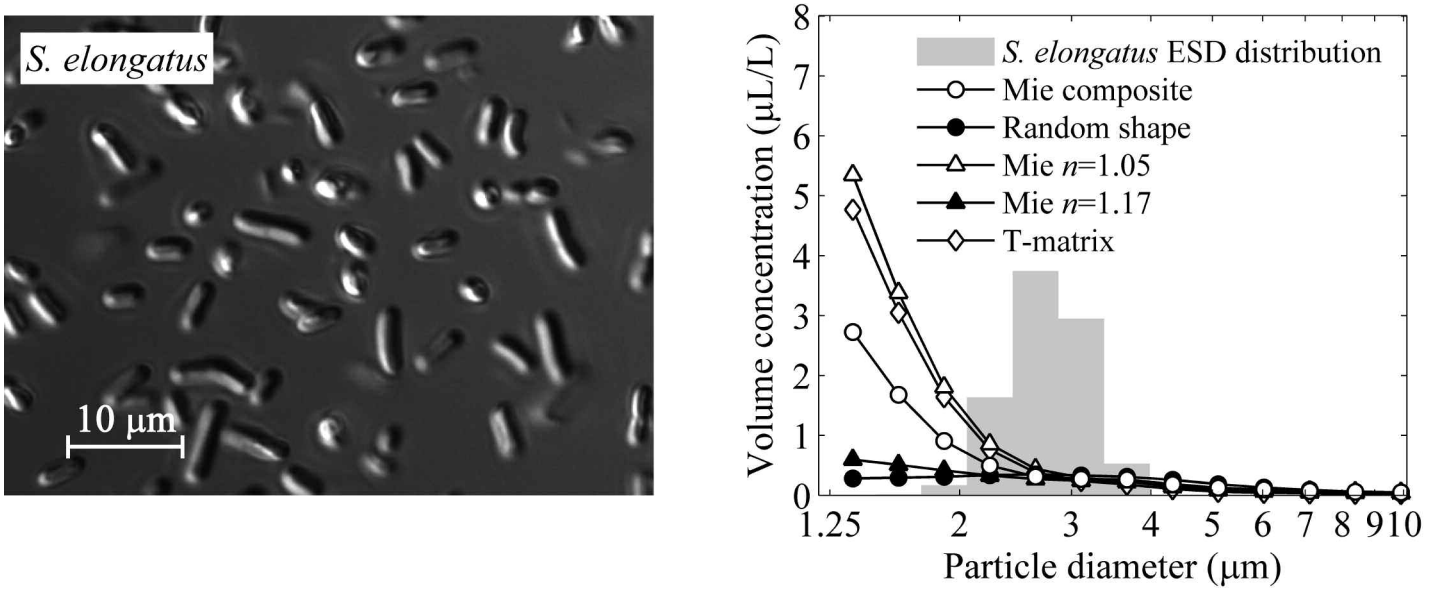

Fig. 7. Cyanobacteria *S. elongatus* culture image and PSD results. Microscope results are shown as shaded bars, and laser diffraction results are shown as processed with three matrices derived from Mie theory, as described in Fig. 3. Assuming spherical particles, one matrix created assuming random shaped particles, and one matrix created assuming small ellipsoid particles using *T*-matrix theory.

of the chain colony, did not produce a noticeable signal in the PSD. All kernel matrices produced similar PSDs, although the random shape matrix did not record most of the local maxima associated with prominent cell dimensions.

Natural particle distributions—To test the effects of kernel matrix processing on natural particle distributions, field samples were collected from the Lake Tahoe watershed, located on the California-Nevada border, USA. Lake Tahoe is a large, oligotrophic mountain lake known for its exceptionally clear water. The water clarity at Lake Tahoe, however, has been decreasing steadily since long term monitoring began in the late 1960s (Jassby et al. 1999). The change is significant, and is believed to be due to accelerated inputs of fine inorganic sediment and algal growth stimulating nutrients to the lake (Reuter et al. 2003). Management strategies addressing the clarity decline depend critically on accurate knowledge of the fine particle size distributions within the lake and watershed, making this an ideal location to examine LISST data processing effects.

The first natural particle sample was composed of fine road dust collected by a vacuum-assisted dry street sweeper in Washoe County, Nevada on 25 Mar 2009. This sample represents particles available to be entrained in urban stormwater runoff and which are believed to play a disproportionately large role in affecting lake clarity (Swift et al. 2006). The road dust was dispersed into ultrapure water, energetically stirred, and LISST measurements and microscope images were taken as described for the bead samples. A second set of natural particle samples were taken from within Lake Tahoe. Samples were obtained using a Van Dorn sampler at 0, 2.5, and 4 m depths on 9 Mar 2009 in Marla Bay, a shallow embayment located in the southeast corner of the lake. The samples were transported back to a laboratory where they were run on the LISST in benchtop mode. At that time, a 100 mL aliquot was taken from each sample, preserved using Lugol's solution, and allowed to settle through a 21 cm high settling column over a period of 3 d. This was done to concentrate the very low particle concentrations found in Lake Tahoe to levels acceptable for microscope image analysis. Microscope images were processed to obtain PSDs, which were then scaled to LISST attenuation values using equation 6 and a constant extinction efficiency of 2. This value is more representative of light attenuation by a wide polydispersion of natural irregular particles than values predicted by Mie theory for any single refractive index (Hodkinson 1963; Proctor and Barker 1974; Bricaud and Morel 1986). Although Lake Tahoe water is very clear in general, these samples were within the upper limit of transmission values (98%) recommended by Sequoia Scientific for accurate LISST measurements.

Because of the wide range of particle sizes in the environmental samples, microscope images were taken at both 100× and 400× magnifications. The high magnification images allowed the image processing routines to more accurately size small particles. The low magnification images had a field of view large enough to encompass the largest particles in the distribution. Separate PSDs were obtained from 20–30 images taken at each magnification and were matched using intermediate-sized particles. In creating the final PSD, large diameter particle concentrations were used from the low magnification images and small particle concentrations were used from the high magnification images.

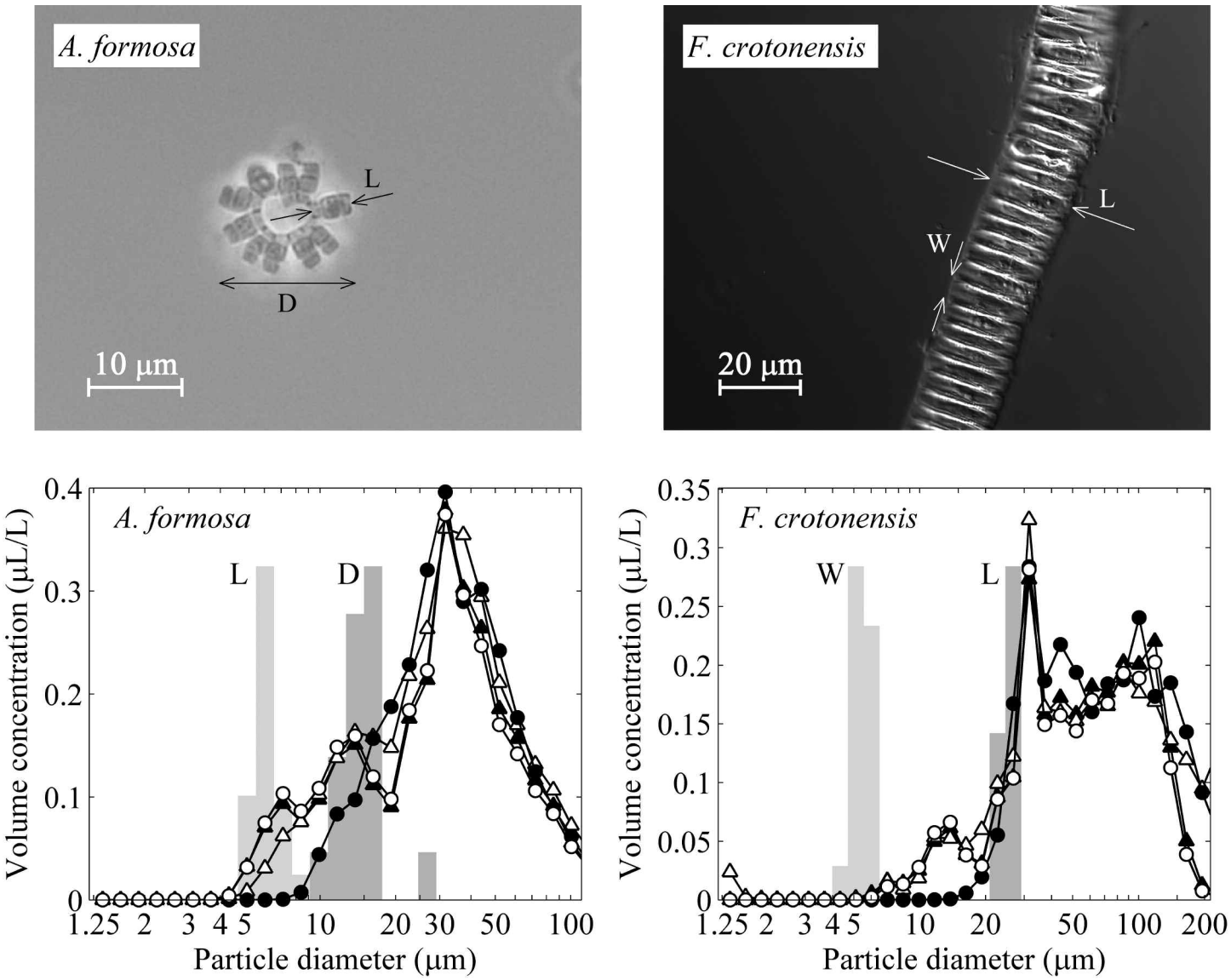

Fig. 8. Bottom: PSDs obtained for chain-forming diatom cultures using LISST laser diffraction data processed with kernel matrices as described and labeled in Fig. 3. Microscope results for the distribution of cell lengths (L) and colony diameters (D) are shown on the left for *A. formosa* as shaded bars. Microscope results for *F. crotonensis* cell lengths (L) and widths (W) are shown on the right. For both species, microscope results are intended to show the relative size distribution; concentration magnitudes should be ignored. Top: Photos show typical colony shapes and define relevant dimensions.

The road dust sample showed a broad particle distribution, centered around 20 µm and spanning the majority of the LISST measurement range (Fig. 9). Even though the particles were overwhelmingly composed of irregular shaped mineral grains, the spherical based matrices produced similar results to the random shape matrix. As with the previous samples, the n = 1.05 and composite matrices invented significant concentrations in the smallest size bins.

Particles in the Marla Bay field sample were a mix of organic phytoplankton and inorganic mineral sediment. Volume concentrations were much lower than the other samples tested in this study, and the PSD was more complicated (Fig. 9, shown for a sample depth of 4 m; other depths were similar). Fine particle concentration increased gradually with increasing diameter from 1.25 µm to approximately 4 µm, with a local maximum at 3 µm; thereafter, a broad peak with many local minima and maxima was seen. The random shape matrix produced the least accurate PSD shape, underestimating all of the concentrations in size bins below 7 µm and creating a sharp peak at 10 µm that was absent from the microscope data. The other three matrices overestimated the 3 µm peak, and the n = 1.05 and composite matrices located it one bin too small. All matrices generally underestimated concentrations in the 4–25 µm size range, with the n = 1.05 matrix

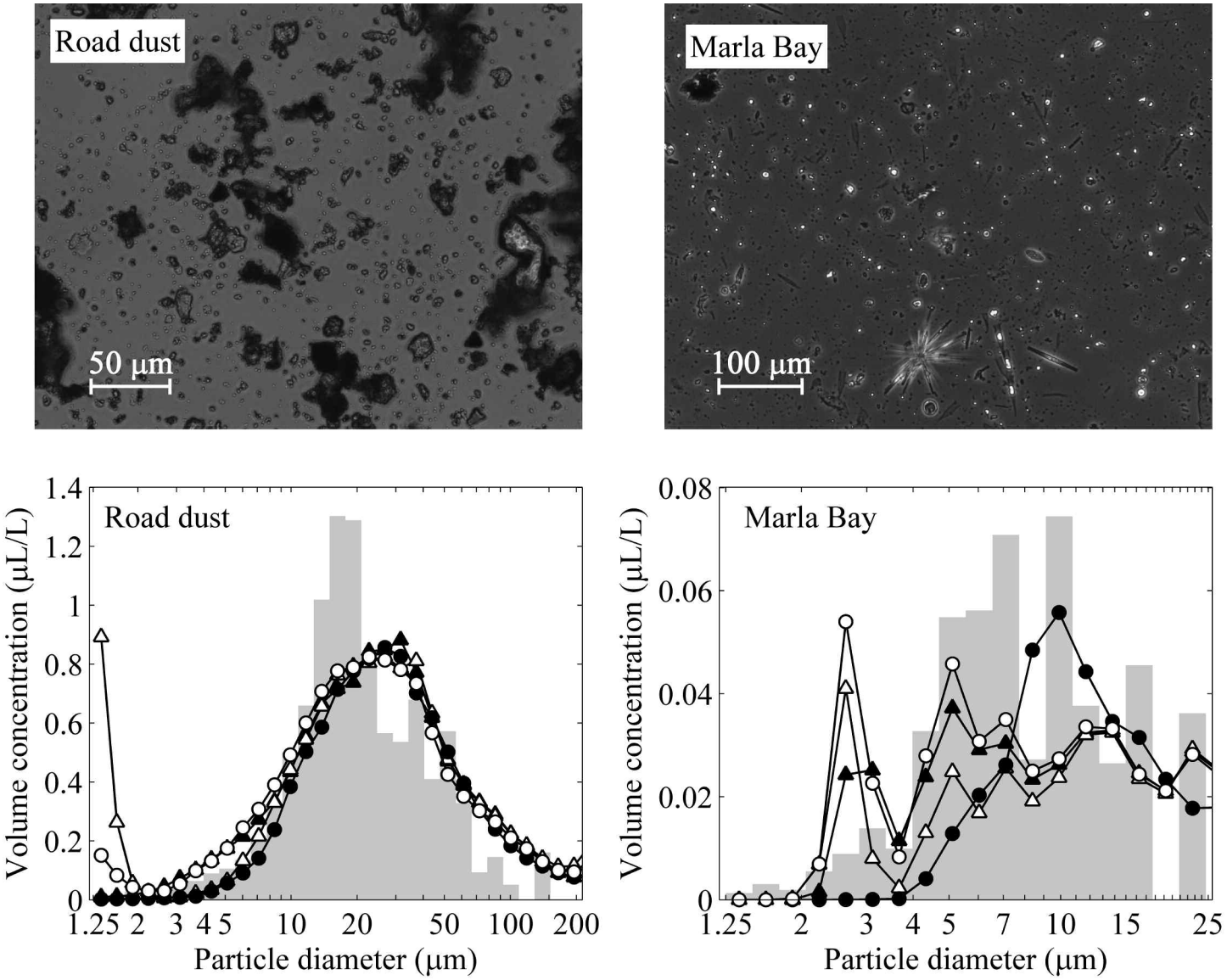

Fig. 9. Bottom: PSDs obtained for natural particle samples using microscopy (shaded bars) and LISST laser diffraction data processed with kernel matrices as described and labeled in Fig. 3. Road dust collected from a Washoe County, Nevada, street sweeper is shown on the left, and a sample from Marla Bay, Lake Tahoe, California-Nevada, is shown on the right. Top: Photos show typical particle shapes and relative size distributions.

underestimating the most. LISST to microscope total volume and area concentration ratios, averaged over both field samples, are given in Table 3 along with values from the bead and phytoplankton culture samples. Field sample volume concentrations measured with the LISST were generally lower than microscope concentrations.

Out-of-range particles—An analysis was conducted on the Tahoe field samples to examine the response of the LISST to particles outside its measurement range. Although it is acknowledged that particles beyond the instrument size limits affect the concentrations of the nearest measureable size bins (Agrawal and Pottsmith 2000; Agrawal et al. 2008), no work quantifying these effects has been done for the LISST. The objective of these experiments is to assess the fraction of out-of-range particles that leak into LISST size bins as a function of the concentration of out-of-range particles present and of the shape of the PSD. To this end, the following steps were taken. (1) The scattering signature across all 32 LISST ring detectors was calculated for one size class of inorganic particles (m = 1.17 + 0.0001i) in the range 1.06–1.25 µm using Mie theory. equation 5 was used in a manner analogous to the way the kernel matrix entries were calculated. The range 1.06–1.25 µm was chosen to preserve the geometrically spaced size bins. A second scattering signature was created in the same way for particles above the upper LISST measurement limit, in the range of 250 to 295 µm. (2) The n = 1.17, LISST-derived PSDs

Table 3. Ratios of LISST total volume concentration to microscope total volume concentration (VCR) and LISST total cross-sectional area concentration to microscope total cross-sectional area (ACR), grouped by sample type.

	Microspheres		Spherical algae		Ellipsoidal algae		Field samples	
	VCR	ACR	VCR	ACR	VCR	ACR	VCR	ACR
Mie composite	1.47	1.82	2.13	2.25	0.81	3.46	0.94	1.11
Random shape	0.96	0.78	1.08	0.86	0.34	0.98	0.77	0.56
Mie n = 1.05	1.90	3.07	4.29	4.48	1.42	6.50	0.86	1.34
Mie n = 1.17	1.08	1.10	0.98	1.00	0.36	1.23	0.88	0.88

for both the road dust and Marla Bay samples were converted back to their corrected scattered power distributions using equation 3. The n = 1.17 results were used because they showed the closest match to the microscope results. (3) A volume concentration was assumed for the out-of-range particles, and the light scattered as a result of that concentration was calculated by multiplying the scattering signature calculated in (1) by the assumed concentration and the volume conversion constant (as in equation 3). Although the conversion constant is not applicable to measurements outside the LISST range, it is expected to give a reasonable approximation for particles very close to LISST limits. Concentrations of approximately 25%, 50%, 75%, and 100% of the average class volume concentration were used for the out-of-range particles. (4) The scattered power distributions calculated in (3) were added to the distributions calculated in (2), and the result was re-inverted using equation 5 to obtain a PSD, which included the influence of various concentrations of out-of-range particles. Unfortunately, the modified Chahine inversion algorithm used in this study includes a smoothing function. This is necessary to provide stable solutions, but means that a PSD containing sharp peaks, when converted to the scattered power distribution and then re-inverted, will have the peaks smoothed out. To account for this smoothing effect, the scattered power distributions calculated in (2) were re-inverted as a control, and the effects of the out-of-range particles were calculated as deviations from this control.

Out-of-range particles of concentration 0.15, 0.3, 0.45, and 0.6 µL/L were simulated for the road dust sample, and concentrations of 0.01, 0.02, 0.03, and 0.04 µL/L were used for Marla Bay. Fig. 10 shows the original PSDs along with the effect of adding either fine or coarse out-of-range particles. Since the PSD responses were found to be proportional to the added concentration, only the highest concentration additions are shown. Although the original PSDs for the road dust and Marla Bay were shaped differently, the out-of-range particle effects were similar. Additions of coarse particles affected the PSDs only slightly, with the greatest deviations seen in the largest size classes, as expected. LISST volume concentrations increased by only 5% to 10% of the volume of the coarse particles added, although this occurred for the largest eight size classes. Fine, out-of-range particles affected the entire PSD. On average, 43% of the simulated fine particle concentration leaked into the first LISST size bin. Twenty-six percent was leaked into the second LISST size bin. Concentrations of particles between 2.5 and 7 µm decreased, some by as much as 30% of the added out-of-range volume concentration. Paradoxically, the concentrations of the largest particle size classes also increased with the fine particle additions, although the response was different for the two PSDs. Volume concentrations in the largest road dust classes increased on average by 11% of the added fine particle volume, whereas those in the Marla Bay sample increased by 35%. To validate these theoretical processing results, we revisited results from the picophytoplankton *P. fluorescens*, which contained significant concentrations of out-of-range fine particles. Increases in the concentration of the first size bins were obscured by index of refraction processing effects, and concentrations in the 2.5–7 µm range were close to zero to begin with, leaving no room for decrease. We did observe a small increase in the largest size bin concentrations beyond what was measured in the microscope results. However, it represented only about 10% of the concentration in the 1.06–1.25 µm range.

Discussion

Inversion of light scattered by fine (<20 µm) particles to obtain a PSD is inherently difficult. The finest fraction of the LISST inversion range displays the largest dependence on index of refraction (Fig. 1) and the largest effects due to polarization of source light (Slade and Boss 2006). These particles also show the least structure in their forward volume scattering functions (Fig. 2), making accurate inversion difficult, are preferentially influenced by fine particles outside the LISST's lower size range, and scatter at wide angles that are more likely to be influenced by particle nonsphericity (Liu et al. 2003). Nevertheless, the under 20 µm size range is important to aquatic scientists optically, biologically, and chemically, and forward scattering measurements within the LISST's angular range should be able to provide a useful characterization of them.

Glass bead samples—Glass microspheres are an excellent material with which to examine kernel matrix index of refraction effects. For solids beads, the material composition is homogeneous and particles are near perfect spheres (results from our bead images indicated average bead convex cross-sectional area to cross-sectional area ratios > 0.98). Scattering by surface irregularities is expected to be low for smooth

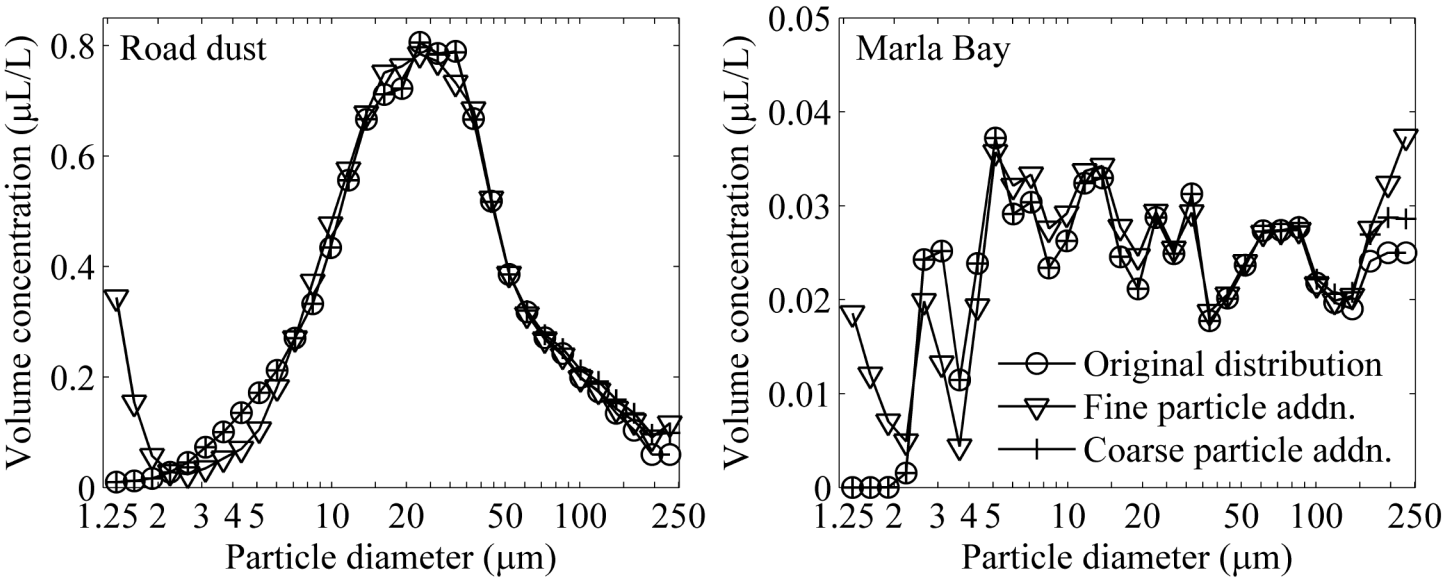

Fig. 10. Effect of out-of-range particles on processed LISST data. Simulated additions of 0.6 µL/L of fine or coarse particles are shown for the road dust sample (left), and 0.04 µL/L additions are shown for the Marla Bay sample (right). Results highlight the complicated effect of out-of-range fine particles on LISST concentrations.

beads, and previous research has shown scattering by surface roughness of particles in general to be of negligible importance (Mühlenweg and Hirleman 1998). We can therefore reliably attribute the invention of small particles in the n = 1.05 and Mie composite matrix bead results to a mismatch in the assumed index of refraction. The invention of small particles was not observed in the n = 1.17 or random shape matrix results, and can be explained by examining the kernel matrices (Fig. 2). The peak scattering magnitudes for the smallest size classes (located at the highest ring numbers) are much lower in the n = 1.05 and composite matrices. Light incident upon the widest ring detectors is thus erroneously interpreted as the result of many small particles, each producing a small amount of scattered light, instead of only a few small particles, each with larger scattering magnitudes. The invention of small particles from the Mie theory composite matrix has previously been documented in results by Agrawal and Traykovski (2001) and Traykovski et al. (1999), but has been attributed to particle shape effects resulting from the processing of natural sediments using a spherical-based matrix (Agrawal et al. 2008). Although shape effects may also be responsible for inventing small particles in natural samples, they can be ruled out for the microsphere bead results seen here. Processing with the n = 1.05 matrix produced the largest number of erroneous small particles, whereas the n = 1.17 matrix, which represented a much closer match to the bead index of refraction, produced the fewest. The matrix created using Mie theory with an average of refractive indices produced intermediate numbers of erroneous particles.

The oversizing of the glass beads using the random shape matrix may also be explained by examining the kernel matrices in Fig. 2. The random shaped particles examined by Agrawal et al. (2008) showed peak scattering 1 to 2 ring detectors smaller than their spherical counterparts. Thus when used on spherical particles, the random shape matrix interprets the scattering distribution as one caused by a slightly larger size class. Poor performance of a matrix designed for random shaped particles on spherical beads is to be expected.

The impact of accuracy in the smallest size bins should not be understated. As was previously noted, an average of 24% and 6.5% of the sample volume was incorrectly created in the 5 µm and 8 µm bead results for the n = 1.05 and Mie theory composite matrices, respectively. These percentages are small when considering the PSD using the LISST default units of volume concentration, but become significant when other unit measures are considered. Total particulate cross-sectional area of a sample is an important measure used in predicting light extinction and the optical characteristics of natural water bodies (Mobley 1994). Forward scattering is most sensitive to this concentration description, and it can be obtained from the volume concentration by dividing each bin by its mean diameter, under the assumption that the particles are spherical. If units of cross-sectional area per volume are considered, an average of 64% and 26% of the total area is erroneously created using the n = 1.05 and composite matrices, respectively. Particle number concentration is another way of specifying the size distribution, which has important applications to aquatic toxicology. Many aquatic species show adverse effects in response to the total number of particles to which they are exposed, not the total mass or volume of those particles (Kühnel et al. 2009). If the number concentrations of the beads are considered, the erroneous small particles dominate the distri-

bution, with an average of 97% and 83% of the total for the $n = 1.05$ and composite matrices, respectively. For applications where the cross-sectional area concentration or number concentration is preferred, results processed with the Mie theory $n = 1.17$ matrix are superior.

Phytoplankton cultures—Analysis of LISST phytoplankton culture results involves several complicating factors, in comparison with the glass bead samples. Particles are no longer homogeneous. Algal cells have a bounding cell wall, membrane, or shell (in the case of coccolithophores) comprised of higher refractive index material than the cell interior (Aas 1996). Cell interiors have chloroplasts and other organelles distributed non-uniformly within low refractive index cytoplasm. This heterogeneity is known to affect the light scattering properties of cells, especially when cells contain gas vacuoles (Volten et al. 1998). Particles are also no longer spherical. Even species described as spherical have aspect ratios that deviate from 1.0 by 10% to 20% [results from this study, Karp-Boss et al. (2007)]. Nonsphericity is known to impart a bias to the inversion process. The LISST and all laser diffraction instruments that measure forward scatter are most responsive to the cross-sectional area of particles within the sampling chamber. However, LISST results are given in default units of volume concentration. These are more easily related to the conserved quantity mass and are of greater use to sediment transport studies for which the LISST was originally designed (Agrawal and Pottsmith 2000). We assume that nonspherical particles in suspension are randomly oriented and therefore a range of the available cross-sectional areas are sampled. This leads us expect a broader distribution in the LISST PSD than if the LISST were most sensitive to particulate volume. Theoretical work on irregular particles by Al-Chalabi and Jones (1994) and on ellipsoids by Matsuyama et al. (2000) suggests this is the case, and scattering from monodisperse nonspherical samples can be accurately modeled using a polydispersion of similar refractive index spheres.

Factors related to sample handling and instrumentation may contribute to discrepancies in comparing LISST and microscope results. Many of these were described in detail by Karp-Boss et al. (2007), but are repeated here for completeness. (1) Microscope results are based on a sample size at least an order of magnitude smaller than the number of particles measured by the LISST. (2) Whereas particles in the LISST sample chamber may be oriented in any random direction, particles observed under the microscope will usually lay flat. This will increase the microscope detected diameters relative to the LISST. (3) Cultures will inevitably contain some bacterial cells, detritus, and/or inorganic particles, which will contribute to light scattering. Particles large enough to be in the LISST inversion range were characterized in the microscope results; however, particles below 1.25 μm will likely produce effects on the LISST PSD in a manner similar to our results for fine out-of-range particles. Concentrations in the first few bins will increase, and concentrations in some intermediate size bins will decrease. The same effect will not be realized in the microscope results. We took care to minimize these effects, and concentrations in the smallest microscope bins suggest out-of-range particles are scarce, but some small sample contamination is no doubt likely. (4) Dilution of the phytoplankton cultures with ultrapure water creates an osmotic gradient that may alter the size of the LISST-measured cells in comparison with the microscope samples. This effect can be assessed by examining the diluted samples under the microscope, although many more digital images must be taken to record a sufficient number of cells. We performed this on a culture of *M. aerginosa* and found no statistically significant difference in the mean particle diameter using a Student t test distribution ($P < 0.05$), but no work was done to test this on the remaining species. (5) Handling and preparation of the microscope samples may disrupt any fragile aggregates that were measured in the LISST samples.

We expected LISST PSDs processed using the organic ($n = 1.05$) kernel matrix to be the most accurate for spherical algae species. This was not found to be the case. The $n = 1.05$ kernel overstated volume and cross-sectional area concentrations, largely as a result of increased concentrations in the smallest bins. Testing with kernel matrices using refractive indices in the range $n = 1.03$–1.07 and absorptive indices in the range 0.002–0.007 produced no significant improvements in the results. We suggest that this response is due to both the nonuniform shape of the algal cells and the heterogeneity of their composition. Nonsphericity of cells may have caused increased light scattered onto the widest rings. Because the nonsphericity of these species is small, we believe the heterogeneity effect is a greater factor. Most algal species have cell membranes or walls comprised of high refractive index minerals, waxes, and oils (Kitchen and Zaneveld 1992). For example, diatoms have amorphous silica frustules ($n = 1.15$) and haptophyte algae are encased in calcium carbonate coccoliths ($n = 1.20$). Although the bulk index of refraction, averaged over the entire cell volume, may be low (Aas 1996), modeling of algal cells as layered spheres, with a high refractive index shell and an absorptive, low index center, suggests that scattering is more complex than the homogeneous, low refractive index model predicts (Kitchen and Zaneveld 1992). Cells with relatively thick outer coverings showed forward scattering at wide angles similar to high refractive index homogeneous spheres. Cells with thinner coatings behaved similarly to low refractive index spheres, but still scattered greater light at wide angles. In this study, several algal classes were considered, with varying wall thicknesses, and all phytoplankton results indicate that a high refractive index model more accurately represents light scattered at small forward angles (0.07°–14.2°) than a low refractive index model.

None of the kernel matrices tested produced accurate results on the ellipsoidal *Synechococcus elongatus* sample. However, we note the similarity between the shape of the results for the *S. elongatus* sample and the 2 μm bead sample. Laser diffraction

data from ellipsoidal particles, processed using a spherical based matrix, can often produce double scattering peaks, provided there is sufficient separation between the major and minor axis lengths (Mühlenweg and Hirleman 1998; Matsuyama et al. 2000). However, analytical results from Matsuyama et al. (2000) on randomly oriented ellipsoids, which represent the conditions in the LISST sampling chamber, indicate a single scattering peak will be seen at the location of the minor axis length. If the scattering peak in *S. elongatus* was equivalent to the minor axis dimension (2.0 µm), we would expect a similar result to that seen on the 2 µm bead sample; this was the case, with both LISST-derived distributions exhibiting a rising fine particle tail. We suspect that the inability of the LISST to record peak concentrations in bins adjacent to the smallest size bin is due to the inversion algorithm, which includes a smoothing function and may smooth PSDs near distribution edges. Processing of the 2 µm bead results using both the Chahine inversion algorithm, supplied by Sequoia Scientific, and the projection method described by Pedocchi and Garcia (2006b) is shown in Fig. 11. The projection method is able to locate the peak diameter outside the first bin, although results are still one bin too small. PSDs presented in this paper were not processed using the projection method because of instability in the method for more complicated PSDs.

Chain-forming diatom species have been previously studied using the LISST by Karp-Boss et al. (2007). For the two diatom species they examined (*Skeletonema costatum* and *Stephanopyxis turris*), multimodal results were observed with maxima at prominent cell dimensions. This is similar to results presented here, although one peak in our *F. crotonensis* sample was not associated with a particular cell dimension. PSD peaks at very large diameters were likely associated with cell chain aggregates that were broken up during microscope sampling preparation. These peaks were very broad and are a likely consequence of the LISST sampling a range of cross-sectional areas associated with a complex aggregate.

Natural particle samples—Natural particle samples are subject to many of the same analysis complications as the phytoplankton cultures. We again expect fine out-of-range particles to be present and influence LISST results but not microscope results. However we expect these influences to be small, because microscope images showed only very low particle concentrations in the finest bins. Concentration of the Marla Bay samples though settling over a period of 3 d may have also contributed to microscope–LISST discrepancies. The Lugol's solution used as a preservative may have caused cells to shrink, shifting the microscope derived PSD toward smaller diameters. A detailed study of this effect presented in Menden-Deuer et al. (2001), however, indicated only a small decrease (<10%) in cell volumes associated with Lugol's preservation over a 3-d period similar to ours. Particle aggregation/flocculation may also occur in the settling column due to differential settling rates or changes in the chemistry of the medium. However, for the very low concentrations of particles found in Lake Tahoe samples, we expect this effect to be small.

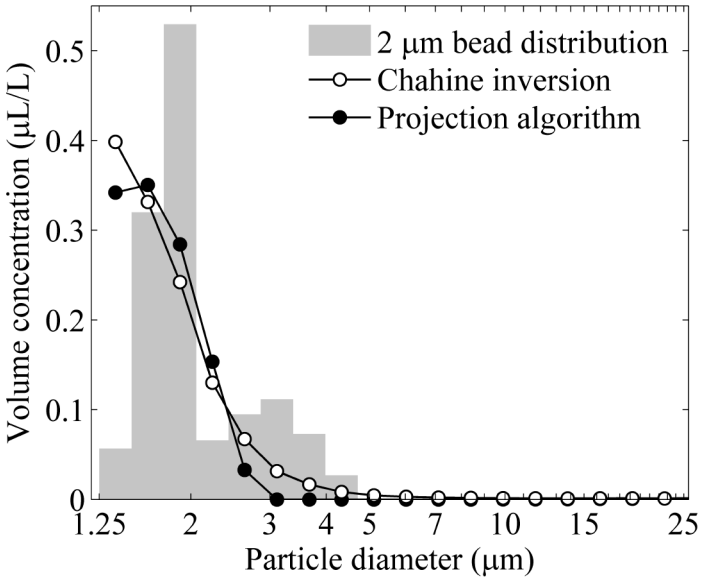

Fig. 11. Effect of inversion algorithm choice. 2 µm microsphere bead results processed with the n = 1.17 kernel matrix using the modified Chahine method and the projection algorithm of Pedocchi and Garcia (2006b).

The natural particle samples largely validated results seen in the microspheres and phytoplankton cultures. Processing with the n = 1.17 matrix produced the most accurate results without creating erroneous concentrations in the smallest size bins. Total volume concentrations were lower in LISST samples than microscope samples, and were likely due to platy mineral particles and broad algal cells laying flat in the microscope samples but having a variety of cross-sectional areas sampled while in the LISST.

Out-of-range particles—Results from the theoretical analysis of particles outside the LISST's inversion range suggest that large particles (above 250 µm) are not a significant source of error. These particles affect only the largest size bins and influence in-range LISST concentrations by only a small fraction (generally less than 10%) of their concentration. Fine, out-of-range particles, however, appear to have a large effect on the LISST. They were found to increase concentrations in the smallest bins sharply, decrease concentrations in the 2.5–7 µm range, and generally affect the full range of the LISST PSD. This presents a large problem for LISST measurements in environments with large concentrations of fine out-of-range particles (e.g., glacial flour or picophytoplankton) are present.

Conclusions, future work, and recommendations

Scattering distributions processed using the matrix derived from Mie theory and assuming an inorganic index of refraction of $m = 1.17 + 0.0001i$ produced the most accurate results in PSD shape and bulk parameters (Table 3) consistently over a wide variety of particle sizes, shapes, and compositions.

Although the matrix was expected to produce accurate results only on samples of inorganic spheres, it performed much better than the organic matrix on phytoplankton samples and produced results no different than the random shape matrix on irregular particles. Importantly, it never suffered from the small particle invention that plagued the Mie theory composite and n = 1.05 matrix results. Accordingly, we recommend use of this matrix over the Mie composite matrix for general environmental samples.

The data processing techniques described here have the advantages of being easy to use and applicable post data collection. equation 4 and the Bohren and Huffman (1983) program, which is widely available, are all that is needed to construct the inorganic n = 1.17 matrix. A Matlab program used to calculate kernel matrices for an arbitrary complex index of refraction and size range is posted at http://terc.ucdavis.edu/research/particlemeasurements.html. Raw scattering distributions do not have to be recollected, only reprocessed with the new kernel matrix, to obtain more accurate results. And whereas it was hypothesized that a priori knowledge of the particle composition was needed to choose the correct processing matrix, results suggest that the inorganic matrix will function adequately for particles covering a wide range of shapes and compositions. It is still suggested, however, that laser diffraction results be combined with microscope techniques when used on natural particle samples, because out-of-range and highly nonspherical particles have been shown to produce inaccurate PSDs. Large out-of-range particles do not present a problem, but particles beyond the fine end of the LISST measurement range, a common component of aquatic ecosystems (Nomizu et al. 1987), have complicated effects which influence the entirety of the LISST derived PSD.

A few aspects of this research suggest future work. While the inorganic Mie matrix was shown to produce very accurate results on glass beads and generally good results on the remainder of the samples, it remains to be shown that constructing and applying a kernel matrix tailored to specific particle shape and composition will produce more accurate results. Perhaps a more realistic model of spherical phytoplankton scattering, such as the 3-layer model suggested by Kitchen and Zaneveld (1992), will be able to produce more accurate phytoplankton PSDs. This could be of great use in the monitoring of lab cultures or *Microcystis* blooms, for example. *T*-matrix approximation methods hold great promise for the construction of scattering signatures for large nonspherical particles, which may eliminate some of the uncertainties associated with analyzing PSDs from samples with chain- or colony-forming algal species. The possibilities for the use of these techniques in creating water body or regionally specific processing matrices are great, but remain to be proven. The effect of fine particles below the LISST's lower size limit also warrants further study. Lab studies should be performed to validate the theoretical results presented here, and methods for correcting LISST results for the presence of these particles should be explored.

References

Aas, E. 1996. Refractive index of phytoplankton derived from its metabolite composition. J. Plankton Res. 18:2223-2249 [doi:10.1093/plankt/18.12.2223].

Adleman, J. R. 2009. Plasmonic nano particles for optofluidic applications. Ph.D. dissertation, California Institute of Technology.

Agrawal, Y. C. 2005. The optical volume scattering function: Temporal and vertical variability in the water column off the New Jersey coast. Limnol. Oceanogr. 50:1787-1794 [doi:10.4319/lo.2005.50.6.1787].

———, and H. C. Pottsmith. 2000. Instruments for particle size and settling velocity observations in sediment transport. Mar. Geol. 168:89-114 [doi:10.1016/S0025-3227(00)00044-X].

———, and P. Traykovski. 2001. Particles in the bottom boundary layer: Concentration and size dynamics through events. J. Geophys. Res. (C Oceans) 106:9533-9542 [doi:10.1029/2000JC900160].

———, A. Whitmire, O. A. Mikkelsen, and H. C. Pottsmith. 2008. Light scattering by random shaped particles and consequences on measuring suspended sediments by laser diffraction. J. Geophys. Res. (C Oceans) 113 [doi:10.1029/2007JC004403].

Al-Chalabi, S. A. M., and A. R. Jones. 1994. Development of a mathematical model for light scattering by statistically irregular particles. Part. Part. Syst. Charact. 11:200-206 [doi:10.1002/ppsc.19940110306].

Bohren, C. F., and D. R. Huffman. 1983. Absorption and scattering of light by small particles. Wiley & Sons.

Bricaud, A., and A. Morel. 1986. Light attenuation and scattering by phytoplankton cells—a theoretical modeling. Appl. Opt. 25:571-580 [doi:10.1364/AO.25.000571].

Clavano, W. R., E. Boss, and L. Karp-Boss. 2007. Inherent optical properties of non-spherical marine-like particles — From theory to observation, pp. 1-38. *In* R. Gibson, R. Atkinson, and J. Gordon [eds.], Oceanography and marine biology: an annual review. Vol. 45. CRC Press.

Fettweis, M. 2008. Uncertainty of excess density and settling velocity of mud flocs derived from in situ measurements. Estuar. Coast. Shelf Sci. 78:426-436 [doi:10.1016/j.ecss.2008.01.007].

Gartner, J. W., R. T. Cheng, P. F. Wang, and K. Richter. 2001. Laboratory and field evaluations of the LISST-100 instrument for suspended particle size determinations. Mar. Geol. 175:199-219 [doi:10.1016/S0025-3227(01)00137-2].

Hipsey, M. R., J. D. Brookes, R. H. Regel, J. P. Antenucci, and M. D. Burch. 2006. In situ evidence for the association of total coliforms and *Escherichia coli* with suspended inorganic particles in an Australian reservoir. Water Air Soil Pollut. 170:191-209. [doi:10.1007/s11270-006-3010-6].

Hirleman, E. D. 1987. Optical scaling of the inverse Fraunhofer diffraction particle sizing problem: the linear system

produced by quadrature. Part. Charact. 4:128-133 [doi:10.1002/ppsc.19870040127].

Hodkinson, J. R. 1963. Light scattering and extinction by irregular particles larger than the wavelength, pp. 87-100. *In* M. Kirker [ed.], Electromagnetic scattering. Macmillan.

Jassby, A. D., C. R. Goldman, J. E. Reuter, and R. C. Richards. 1999. Origins and scale dependence of temporal variability in the transparency of Lake Tahoe, California-Nevada. Limnol. Oceanogr. 44:282-294 [doi:10.4319/lo.1999.44.2.0282].

Jones, A. R. 1999. Light scattering for particle characterization. Prog. Energy Combust. Sci. 25:1-53 [doi:10.1016/S0360-1285(98)00017-3].

Karp-Boss, L., L. Azevedo, and E. Boss. 2007. LISST-100 measurements of phytoplankton size distribution: evaluation of the effects of cell shape. Limnol. Oceanogr. Methods 5:396-406.

Kitchen, J. C., and J. R. V. Zaneveld. 1992. A three-layered sphere model of the optical properties of phytoplankton. Limnol. Oceanogr. 37:1680-1690 [doi:10.4319/lo.1992.37.8.1680].

Klein, C. 2002. The 22nd edition of the manual of mineral science: (after James D. Dana). Cornelius S. Hurlbut, Jr., with continued contribution of. Wiley.

Kühnel, D., and others. 2009. Agglomeration of tungsten carbide nanoparticles in exposure medium does not prevent uptake and toxicity toward a rainbow trout gill cell line. Aquat. Toxicol. 93:91-99. [doi:10.1016/j.aquatox.2009.04.003].

Liu, L., M. I. Mishchenko, J. W. Hovenier, H. Volten, and O. Munoz. 2003. Scattering matrix of quartz aerosols: comparison and synthesis of laboratory and Lorenz-Mie results. J. Quant. Spectrosc. Radiat. Transfer 79:911-920. [doi:10.1016/S0022-4073(02)00328-X].

Ma, X. Y., J. Q. Lu, R. S. Brock, K. M. Jacobs, P. Yang, and X. H. Hu. 2003. Determination of complex refractive index of polystyrene microspheres from 370 to 1610 nm. Phys. Med. Biol. 48:4165-4172 [doi:10.1088/0031-9155/48/24/013].

Matsuyama, T., H. Yamamoto, and B. Scarlett. 2000. Transformation of diffraction pattern due to ellipsoids into equivalent diameter distribution for spheres. Part. Part. Syst. Charact. 17:41-46 [doi:10.1002/1521-4117(200006)17:2<41::AID-PPSC41>3.0.CO;2-W].

Menden-Deuer, S., E. J. Lessard, and J. Satterberg. 2001. Effect of preservation on dinoflagellate and diatom cell volume and consequences for carbon biomass predictions. Mar. Ecol. Prog. Ser. 222:41-50 [doi:10.3354/meps222041].

Mikkelsen, O. A. 2002. Examples of spatial and temporal variations of some fine-grained suspended particle characteristics in two Danish coastal water bodies. Oceanol. Acta 25:39-49 [doi:10.1016/S0399-1784(01)01175-6].

Mishchenko, M. I., L. D. Travis, and D. W. Mackowski. 1996. T-matrix computations of light scattering by nonspherical particles: A review. J. Quant. Spectrosc. Radiat. Transfer 55:535-575 [doi:10.1016/0022-4073(96)00002-7].

———, and ——— 1998. Capabilities and limitations of a current FORTRAN implementation of the T-matrix method for randomly oriented, rotationally symmetric scatterers. J. Quant. Spectrosc. Radiat. Transfer 60:309-324 [doi:10.1016/S0022-4073(98)00008-9].

Mobley, C. D. 1994. Light and water: radiative transfer in natural waters. Academic Press.

Mühlenweg, H., and E. D. Hirleman. 1998. Laser diffraction spectroscopy: influence of particle shape and a shape adaptation technique. Part. Part. Syst. Charact. 15:163-169 [doi:10.1002/(SICI)1521-4117(199808)15:4<163::AID-PPSC163>3.0.CO;2-8].

Nomizu, T., T. Nozue, and A. Mizuike. 1987. Electron microscopy of submicron particles in natural waters–morphology and elemental analysis of particles in fresh waters. Microchim. Acta 2:99-106 [doi:10.1007/BF01201722].

Pedocchi, F., and M. H. Garcia. 2006a. Evaluation of the LISST-ST instrument for suspended particle size distribution and settling velocity measurements. Cont. Shelf Res. 26:943-958. [doi:10.1016/j.csr.2006.03.006].

——— and ———. 2006b. Noise-resolution trade-off in projection algorithms for laser diffraction particle sizing. Appl. Opt. 45:3620-3628 [doi:10.1364/AO.45.003620].

Proctor, T. D., and D. Barker. 1974. The turbidity of suspensions of irregularly shaped diamond particles. J. Aerosol Sci. 5:91-99 [doi:10.1016/0021-8502(74)90010-X].

Reuter, J. E., and others. 2003. An integrated watershed approach to studying ecosystem health at Lake Tahoe, CA-NV, pp. 1283-1298. *In* D. J. Rapport, W. L. Lasley, D. E. Rolston, N. O. Nielsen, C. O. Qualset, and A. B. Damania [eds.], Managing for healthy ecosystems. Lewis.

Rienecker, E., J. Ryan, M. Blum, C. Dietz, L. Coletti, R. Marin III, and W. P. Bissett. 2008. Mapping phytoplankton in situ using a laser-scattering sensor. Limnol. Oceanogr. Methods 6:153-161.

Riley, J. B., and, Y. C. Agrawal. 1991. Sampling and inversion of data in diffraction particle sizing. Appl. Opt. 30:4800-4817 [doi:10.1364/AO.30.004800].

Shen, J., B. Yu, H. Wang, H. Yu, and Y. Wei. 2008. Smoothness-constrained projection method for particle analysis based on forward light scattering. Appl. Opt. 47:1718-1728 [doi:10.1364/AO.47.001718].

Slade, W. H., and E. S. Boss. 2006. Calibrated near-forward volume scattering function obtained from the LISST particle sizer. Opt. Express 14:3602-3615 [doi:10.1364/OE.14.003602].

Stramski, D., A. Bricaud, and A. Morel. 2001. Modeling the inherent optical properties of the ocean based on the detailed composition of the planktonic community. Appl. Opt. 40:2929-2945 [doi:10.1364/AO.40.002929].

———, E. Boss, D. Bogucki, and K. J. Voss. 2004. The role of seawater constituents in light backscattering in the ocean. Prog. Oceanogr. 61:27-56 [doi:10.1016/j.pocean.2004.07.001].

Swift, T. J., J. Perez-Losada, S. G. Schladow, J. E. Reuter, A. D. Jassby, and C. R. Goldman. 2006. Water clarity modeling in

Lake Tahoe: Linking suspended matter characteristics to Secchi depth. Aquat. Sci. 68:1-15 [doi:10.1007/s00027-005-0798-x].

Traykovski, P., R. J. Latter, and J. D. Irish. 1999. A laboratory evaluation of the laser in situ scattering and transmissometery instrument using natural sediments. Mar. Geol. 159:355-367 [doi:10.1016/S0025-3227(98)00196-0].

Volten, H., and others. 1998. Laboratory measurements of angular distributions of light scattered by phytoplankton and silt. Limnol. Oceanogr. 43:1180-1197 [doi:10.4319/lo.1998.43.6.1180].

Waterman, P. C. 1965. Matrix formulation of electromagnetic scattering. Proc. IEEE 53:805-812 [doi:10.1109/PROC.1965.4058].

Submitted 26 March 2010
Revised 27 July 2010
Accepted 18 August 2010